Role of oxygen functional groups in the friction of water-lubricated low-index diamond surfaces

Takuya Kuwahara,[1] Gianpietro Moras,[1] and Michael Moseler[1,2,*]
[1]*Fraunhofer IWM, MicroTribology Center μTC, Wöhlerstraße 11, 79108 Freiburg, Germany*
[2]*Institute of Physics, University of Freiburg, Hermann-Herder-Straße 3, 79104 Freiburg, Germany*

(Received 2 May 2018; published 18 July 2018)

Large-scale quantum molecular dynamics simulations unveil eight friction regimes of water-lubricated low-index diamond surfaces. Four of these friction regimes are universal, i.e., they occur on diamond (111), (001), as well as (110). Dry sliding leads to immediate cold welding accompanied by amorphization (regime I). Small amounts of water (less than 8 H_2O per nm^2) can preserve crystallinity and lower friction by localizing shear to interfacial ether groups (regime II). A further increase in water surface density results in passivating hydrogen/hydroxyl layers (regime IV) and finally (for more than 20 H_2O per nm^2) in free water layers between hydrogen/hydroxyl passivated diamond surfaces (regime V). The other four friction regimes are special, i.e., they occur only on certain surfaces. An ultralow friction regime is established by aromatic Pandey surface passivation on diamond (111) surfaces (regime III). On diamond (110) surfaces, regime II coexists with three other regimes: while partial cold welding via C–C bonds (regime VI) or C–O–C bonds (regime VII) leads to frictional shear stresses that are in-between the cold-welding regimes (I and II) and the non-cold-welding regimes (IV and V), the formation of an oxidized carbon monolayer consisting of keto and ether groups results in ultralow friction (regime VIII). Regime VIII is also observed for diamond (001) surfaces. These findings are rationalized by the structural and energetic peculiarities of the different low-index surfaces. Our study provides guidelines for nanoscale control and manipulation of oxygen functional groups on carbon surfaces in boundary lubrication with water or other oxygen-containing lubricants.

DOI: 10.1103/PhysRevMaterials.2.073606

I. INTRODUCTION

A fundamental understanding of friction between two solids is a scientific challenge of great importance for a sustainable future of mankind [1]. A drastic reduction of friction in all branches of industry as well as in the transportation sector will result in enormous energy savings and a sizable reduction of CO_2 emission [2]. Despite being a macroscopic property of a tribological system, friction is governed by atomic-scale processes that occur at the sliding interface, such as cold welding (CW) [3], tribo-induced phase transitions [4], contact aging [5], tribochemical reactions [6], and atomic stick-slip [7]. Such a variety of atomic-scale processes yield friction coefficients μ that span more than three orders of magnitude (from superlow $\mu < 0.01$ to superhigh $\mu > 1$). Many powerful experimental techniques to elucidate these processes have emerged over the last years [8,9]. However, buried tribological interfaces are hardly accessible and experimental temporal and spatial resolutions are often insufficient to unambiguously identify the elementary friction mechanisms. Therefore, experiments are often complemented by atomistic simulations in order to gain a deeper understanding of the physical [10] and chemical [11] interactions between two sliding surfaces and of the resulting, shear-induced structural transformations [4,5,11]. These studies indicate that surface passivation is a key concept for ultralow friction, since the elimination of strong chemical interactions between two sliding bodies represents a prerequisite to achieve $\mu \sim 0.01$. As a result, a growing number of experimental and theoretical studies have lately been devoted to the formation of passivation layers originating from lubricants [12] or environmental gases (e.g., oxygen and water vapor) [13,14].

The friction between diamond-coated surfaces in a humid environment is an interesting example of how tribochemically induced surface passivation can significantly alter the tribological performance of a technological material. Single-crystal and polycrystalline diamond coatings have excellent mechanical hardness, thermal conductivity, and chemical inertness, which make them an important tribomaterial for bearing [15] and seal applications [16]. Clean diamond surfaces sliding against each other under vacuum conditions exhibit very high friction ($\mu \sim 1$) [17], resulting in amorphization [4] and considerable wear [13]. Remarkably, friction coefficients drop by two orders of magnitude when the diamond/diamond tribointerface is exposed to dry air with relative humidity (RH) of about 1% [13,14]. In particular, after an initial running-in period, during which the passivation of reactive surfaces resulting from high-pressure contacts between asperities takes place, a transition from high to ultralow friction occurs [14,18]. Konicek *et al.* [18] observed spectroscopic fingerprints of C–O and C=O bonding, such as hydroxyl (C–OH), ether (C–O–C), and keto (C=O) groups, on ultrananocrystalline diamond (UNCD) surfaces after running-in with water.

Quantum-mechanical (QM) calculations [11,19] confirmed that water molecules confined between two diamond surfaces split into hydrogen atoms and hydroxyl (OH) groups that chemisorb on the surfaces and passivate dangling bonds (DBs).

*Corresponding author: michael.moseler@iwm.fraunhofer.de

Furthermore, other carbon-oxygen groups (e.g., ether groups and keto groups) and even water-induced aromatic structures were recently found to play a crucial role in the friction behavior of (111) diamond surfaces [11]. The formation of such carbon-oxygen chemical groups and surface reconstructions, their tribological evolution, as well as their effect on friction deserve a deeper investigation as they significantly depend on the diamond surface orientation. Since microcrystalline diamond (MCD) coatings are terminated by low-index facets, i.e., (111), (110), and (001) [15], understanding surface-orientation effects is crucial to predict their frictional properties. Indeed, low-index diamond surfaces have different chemical reactivity and surface reconstructions that are dictated by the specific configurations of surface C atoms and might be related to diamond's friction anisotropy, which has fascinated scientists since the 1950s [17,20,21]. As the anisotropy persists even when the diamond surfaces are contaminated by oxygen and water vapor [21], the H_2O/diamond reaction layers must be very thin (most likely monolayer thick) and retain features of the underlying surface orientations.

In this article water-lubricated, low-index diamond surfaces are studied employing molecular dynamics (MD) simulations with the self-consistent-charge density-functional-based tight-binding (SCC-DFTB) method [22,23] as well as density-functional theory (DFT) molecular statics [24] simulations. The DFTB-MD method allows for a direct exploration of the structural evolution of the sliding interface and the resulting friction. The DFTB findings are corroborated by high-accuracy DFT calculations of the diamond/water interaction. The three prominent low-index surfaces (111), (110), and (001) are considered, since they are dominant in MCD coatings and have been extensively investigated [25–27]. For each surface orientation, sliding simulations are performed in two sliding directions perpendicular to each other. A study of the frictional behavior of diamond for increasing quantities of water allows for a systematic mapping of friction regimes. The emergence of different oxygen functional groups, their evolution, and their effect on friction is presented for each surface and friction regime. Although focused on water lubrication, this study provides basic stimuli for further research on friction mechanisms of oxidized carbon surfaces in boundary lubrication with base oils, like, e.g., oleic acid [12] and glycerol [28].

II. METHODS

In our DFTB models, the system consists of two diamond (111), (110), or (001) slabs that initially confine a given amount of water molecules n_{H_2O}. The two outermost surfaces of the slabs are hydrogen passivated. A carbon layer at the bottom of the lower slab is held rigid, while a top carbon layer of the upper slab is rigidly moved at a constant velocity of $v = 100$ m/s and loaded with a normal pressure P_N of 5 GPa [29]. The equations of motion are integrated using a velocity Verlet algorithm with a time step of 0.5 fs [30]. The system temperature is kept constant at 300 K using a Langevin thermostat acting perpendicular to the sliding direction [31].

The following system sizes are used in the DFTB simulations: $l_x = 0.87$ nm, $l_y = 0.76$ nm, $l_z = 5.00$ nm, $n_C = 288$, $n_H = 24$ for (111); $l_x = 0.71$ nm, $l_y = 0.76$ nm, $l_z = 5.00$ nm, $n_C = 240$, $n_H = 24$ for (110); $l_x = 1.01$ nm, $l_y = 0.76$ nm, $l_z = 5.00$ nm, $n_C = 288$, $n_H = 24$ for (001). Here l_x and l_y represent the lateral periodic box size in and perpendicular to sliding direction, respectively. l_z is the vertical size of the simulation box. n_C and n_H denote the number C atoms and passivating H atoms in the samples, respectively. For each surface orientation, the upper surface is moved along two different directions: $x = \langle 11\bar{2}\rangle$ and $y = \langle 1\bar{1}0\rangle$ for (111); $x = \langle 001\rangle$ and $y = \langle 1\bar{1}0\rangle$ for (110); $x = \langle 110\rangle$ and $y = \langle 1\bar{1}0\rangle$ for (001).

During the simulation, the forces on the upper rigid layer provide the evolution of the systems' frictional force $F_F(t)$. After a running-in period $t_0 = 0.1$ ns, $F_F(t)$ is averaged during time intervals $t_x = \frac{l_x}{v}$ to obtain short time averages $\langle F_F\rangle_m = \int_{t_0+(m-1)t_x}^{t_0+mt_x} F_F(t)dt$. A mean friction force $\langle F_F\rangle$ and a standard deviation of the mean are calculated by further averaging over five t_x periods ($m = 0, \ldots, 4$). The mean friction force is used to determine the frictional shear stress $\sigma = \frac{\langle F_F\rangle}{l_x l_y}$ and the friction coefficient $\mu = \frac{\sigma}{P_N}$.

DFT calculations are carried out using the projector augmented wave method [32] with the Perdew-Burke-Ernzerhof generalized gradient approximation [33] to the exchange-correlation functional as implemented in the Quantum ESPRESSO software suite [24]. The cutoff energies for the plane-wave basis and charge density are set to be 40 and 320 Ry, respectively. Electronic k points are sampled with a $2 \times 2 \times 1$ Monkhorst-Pack grid [34]. Structural optimizations are performed until the atomic forces are less than 5×10^{-4}a.u.

It is instructive to discuss differences in the sliding velocities and contact pressures between experiments and our atomistic simulations as well as a rationale for the use of a thermostat. Typical macroscopic contact pressures are on the order of 100 MPa [13]. However, on the nanoscale, a few major asperities support much higher contact pressures (> 1 GPa) [25], whereas most of the asperities are not in contact and separated by a large gap. Such asperity contacts dominate the frictional behavior, and as a result, lead to surface smoothening, wear, and mechanochemical reactions [35,36]. Therefore, we use a contact pressure P_N of 5 GPa in this study.

Due to the excessive computational costs of QM simulations, high sliding speeds are necessary in order to be able to simulate a long sliding distance and to sufficiently sample phase space. In principle, one must keep the sliding speed well below the speed of sound in materials. The speed of sound in diamond is 100–200 times larger than sliding speed of 100 m/s used in our simulations. This ensures that the heat generated in contact during sliding is rapidly dissipated from the sliding interface to surrounding materials. The criterion is a prerequisite for reliable modeling of the shear response of materials and in this sense our simulations are sound. Importantly, typical sliding speeds in seal applications can be of the order of 10 m/s and more [16], and therefore our models are relevant to realistic applications of microcrystalline diamond coatings.

In experimental tribosystems, the asperities are connected to the body of the coating which forms a heat bath. Due to the limitations caused by the high computational cost of QM simulations, our model does not explicitly include a heat flow from the sliding interface between two asperities into surrounding materials. Instead, the degrees of freedom of the material that supports the asperities are projected out of Newton's equation

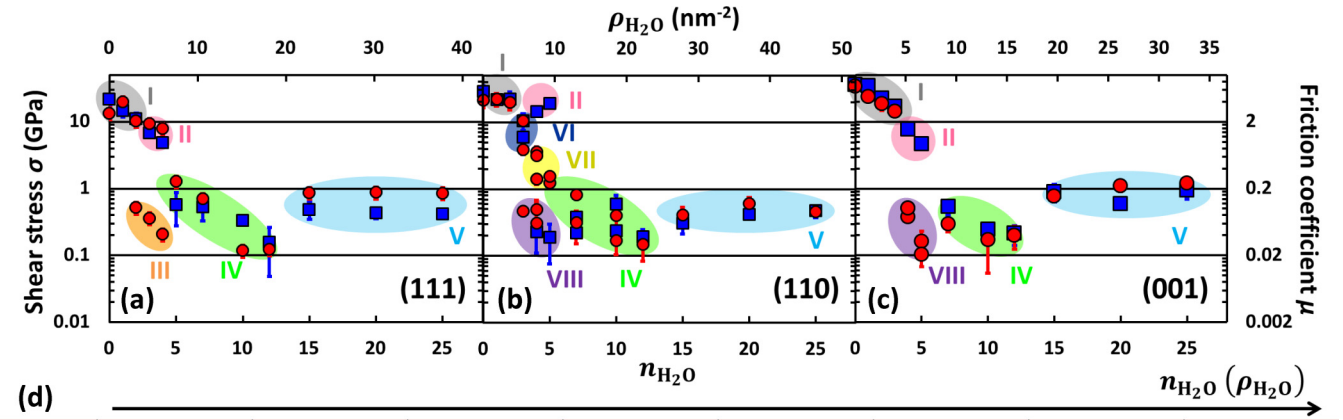

Friction regime	I Harsh CW & Amorphization	VI Mild CW & Amorphization	II Harsh ether-CW	VII Mild ether-CW	III Aromatic passivation	VIII Keto/ether passivation	IV Hydroxyl passivation	V Water film
(111)	Yes	No	Yes	No	Yes	No	Yes	Yes
(110)	Yes	Yes	Yes	Yes	No	Yes	Yes	Yes
(001)	Yes	No	Yes	No	No	Yes	Yes	Yes
⟨s⟩⟨d⟩	(110)⟨001⟩	(110)⟨001⟩	(110)⟨1$\bar{1}$0⟩	(110)⟨001⟩	(111)⟨11$\bar{2}$⟩	(001)⟨110⟩	(001)⟨1$\bar{1}$0⟩	(110)⟨1$\bar{1}$0⟩

FIG. 1. Frictional shear stress σ and friction coefficient μ as a function of the number of confined water molecules n_{H_2O} and water surface density ρ_{H_2O} for (a) (111), (b) (110), and (c) (001) diamond surfaces. (**s**)⟨**d**⟩ denotes the surface orientation and sliding direction, respectively. For each surface orientation, the upper surfaces are moved along two different directions (red circles: x directions, blue squares: y directions). The x and y directions correspond to ⟨11$\bar{2}$⟩ and ⟨1$\bar{1}$0⟩ for (111); ⟨001⟩ and ⟨1$\bar{1}$0⟩ for (110); ⟨1$\bar{1}$0⟩ and ⟨1$\bar{1}$0⟩ for (001). (d) Summary of surface-orientation-dependent friction regimes of water-lubricated diamond surfaces. In the bottom row, representative snapshots for all the friction regimes are shown. While roman numbers I to V (black) are the same as in Ref. [11], novel friction regimes (VI, VII, and VIII) are colored in red. Gray, red, and cyan spheres represent C, O, and H atoms, respectively.

of motion, leading to the Langevin equation that mimics the coupling of atoms to a heat bath [37]. Thermostating the system is essential to model the heat evolution at the sliding interface and the rapid energy dissipation into the surrounding solids without a long-time simulation and the explicit inclusion of a large number of surrounding atoms.

III. RESULTS

DFTB MD simulations of water-lubricated diamond surfaces are performed with a varying number of water molecules n_{H_2O} for (111), (110), and (001) surfaces. Figures 1(a)–1(c) show the shear stress σ and friction coefficient μ as a function of n_{H_2O} (or alternatively the water surface density $\rho_{H_2O} = \frac{n_{H_2O}}{l_x l_y}$). Four universal friction regimes [I, II, IV, and V in Figs. 1(a)–1(c)] are observed. In addition, four surface-dependent friction regimes emerge that are specific for certain surface orientations: III for (111) in Fig. 1(a), VI and VII for (110) in Fig. 1(b), and VIII for (110) and (001) in Figs. 1(b) and 1(c). These eight friction regimes of water-lubricated diamond surfaces and representative atomic structures of the diamond/diamond interface are tabulated in Fig. 1(d). Five of these regimes [I–V in Fig. 1(d)] have already been reported by us for diamond (111) surfaces in a previous letter [11]. In this article we focus on (110) and (001) surfaces and the additional regimes VI–VIII [in red in Fig. 1(d)].

A. Universal friction regimes for (111), (110), and (001) surfaces

Before concentrating on the surface-dependent regimes VI–VIII, the universal friction regimes I, II, IV, and V are briefly described and characterized according to the chemical structure of the tribological interface. Regime I (harsh CW and amorphization) and regime II (harsh ether-CW) belong to the CW regimes with $\mu > 0.2$, while regime IV (hydroxyl passivation) and regime V (water films) are non-CW (NCW) regimes with $\mu < 0.2$. In this section we provide a summary of observations for the universal friction regimes on (111) surfaces (for more details the reader is referred to our previous study [11]) and mention the similarity and dissimilarity to (110) and (001) surfaces when necessary.

1. Harsh CW and amorphization (regime I)

For all three surface orientations, water starvation immediately causes CW via interfacial C–C bonds and a large shear stress ($\sigma > 10$ GPa) which induces amorphization and sp^3-to-sp^2 rehybridization at the interface (regime I in Fig. 1). This process was previously reported by Pastewka *et al.* [4] who employed classical MD with a bond-order potential and observed that the amorphization rate in dry diamond/diamond contacts depends on the surface orientations and sliding directions. In particular, they found that, while the (111) surface is hard to amorphize, the (110) and (001) surfaces easily transform into sp^2-rich amorphous carbon (a-C). Although our QM MD simulations are too short to quantitatively reproduce the previous result, we observe a higher amorphization rate for (110) and (001) surfaces. Interestingly, the presence of a small amount of water ($n_{H_2O} \leqslant 3$) also results in amorphization, producing a thin hydrogenated and oxidized amorphous carbon (a-C:O:H) layer.

2. Harsh ether-CW (regime II)

A slight increase in the number of water molecules ($n_{H_2O} =$ 3 and 4) prevents amorphization and preserves surface crystallinity through the formation of interfacial ether (C–O–C) groups (regime II in Fig. 1). While in regime I the shear strain causes the breaking of interface C–C bonds, in regime II it leads to the breaking and reforming of C–O bonds. The reduced tensile strength of C–O bonds [38] leads to slightly smaller shear stress ($5 \leqslant \sigma \leqslant 10$ GPa) compared to regime I. For (110) and (001) surfaces, this harsh ether-CW friction regime appears only when sliding in the hard $\langle 1\bar{1}0\rangle$ and $\langle 110\rangle$ directions, respectively. Interestingly, for (110) surfaces σ increases with increasing n_{H_2O} and, due to a dense population of interfacial C–O–C groups [Fig. 1(b)], for $n_{H_2O} = 5\,\sigma$ is of the same order of magnitude as the σs in regime I.

3. Hydroxyl passivation (regime IV)

At higher water density ($\rho_{H_2O} \gtrsim 8$ nm^{-2}), the diamond surfaces are sufficiently passivated with H/OH groups and interfacial chemical bonds are prevented. As a result, μ drops to about 0.02 as ρ_{H_2O} increases (regime IV in Fig. 1). For (111) surfaces, this friction regime appears for $5 \leqslant n_{H_2O} \leqslant$ 12, implying that at least 42% of the surface DBs must be passivated with H and OH groups to prevent the formation of covalent bonds across the shearing interface. There is no significant difference between the three low-index diamond surfaces. This suggests that a dense H/OH surface passivation can lead to an ultralow friction regime for any diamond surface orientation and probably also for a-C surfaces [18].

4. Water film (regime V)

In general, the H/OH surface passivation occurs via water splitting into H and OH groups and passivation of two neighboring DBs. However, when surfaces are already sufficiently passivated, the presence of two neighboring DBs becomes less likely. In this case, Grotthuss-type transport of H_3O^+ and OH^- bridges the gap between distant DBs [11]. After saturation of all surface DBs, excess water molecules arrange in layers parallel to the sliding surfaces and constitute a nm-thick additional lubricating film (regime V in Fig. 1 for $\rho_{H_2O} \gtrsim 20$ nm^{-2}). For (111) surfaces with $n_{H_2O} = 25$, a water layer with a thickness of 0.4 nm forms. In this regime, friction coefficients range between 0.05 and 0.2. This elevated friction coefficients can be traced back to the ultrathin thickness of these water films ($h < 1$ nm) and the applied high normal pressure. Water confined in subnanometer channels displays a drastic increase in the viscosity at low sliding speeds ($v < 10$ m/s) and shear-thinning, non-Newtonian behavior, at high sliding speeds ($v >$ 10 m/s) [39,40]. The viscosity also increases with pressure [41]. In contrast, already at $h > 1$ nm and for pressures of the order of several 100 MPa, the viscosity of confined water is almost the same as that of bulk water ($\eta = 0.89$ mPa s) and water behaves as a Newtonian fluid for $v < 100$ m/s. Under such moderate conditions friction coefficients can be estimated using the Newton's law of viscosity. For instance, for $h = 2$ nm, $v = 1$m/s, and $P_N = 100$ MPa, a superlow friction coefficient μ ($= \eta v / h P_N$) of 0.004 is obtained.

B. Surface-orientation-dependent friction regimes

Interestingly, four nonuniversal friction regimes are found for lean water lubrication (regimes III, VI, VII, and VIII for 2 nm$^{-2} \leqslant \rho_{H_2O} \leqslant 10$ nm^{-2}, Fig. 1). All these regimes are strongly influenced by the characteristics of the pristine diamond surfaces and are a consequence of shear-induced C–C bond breaking occurring at interfaces that were initially in a CW regime (regime I or II). This suggests that oxidized tribological interfaces that are in regimes I and II (harsh CW conditions, high friction) can evolve into oxidized interfaces characterized by an ultralow friction regime. The characteristic structural patterns, and in particular the oxygen bonding structures, are presented in this section.

1. Aromatic passivation (regime III)

A shear-induced aromatic Pandey reconstruction of the (111) surface establishes an ultralow friction regime [11]. This reconstruction is unique to the (111) surface and its aromaticity is attributed to delocalized π-bonded chains [42]. The Pandey-reconstructed (111) surface is able to passivate itself and to withstand high tribological loads without any chemical termination by oxygen functional groups or hydrogen. We note that chemical termination with H/OH groups destroys the aromaticity [11]. DFT-MD simulations by Kern *et al.* [43] reported that the Pandey reconstruction is a precursor for larger aromatic structures and elevated temperatures can cause further graphitization on diamond (111) surfaces, e.g., dome-shaped structures and graphene. Sliding contacts of these aromatic surfaces result in superlow friction ($\mu < 0.01$) even in the absence of water [11].

2. Additional friction regimes for (110) surfaces (regimes VI–VIII)

Ether and keto groups that form during sliding govern the frictional behavior of diamond (110) surfaces with lean water lubrication [$3 \leqslant n_{H_2O} \leqslant 5$ in Fig. 1(b)]. Figure 2(a) displays the evolution of the shear stress σ and friction coefficient μ for three MD trajectories (A–C) in which two diamond (110) surfaces slide against each other along the soft $\langle 001\rangle$ direction [4] with $n_{H_2O} = 4$. All trajectories start from the

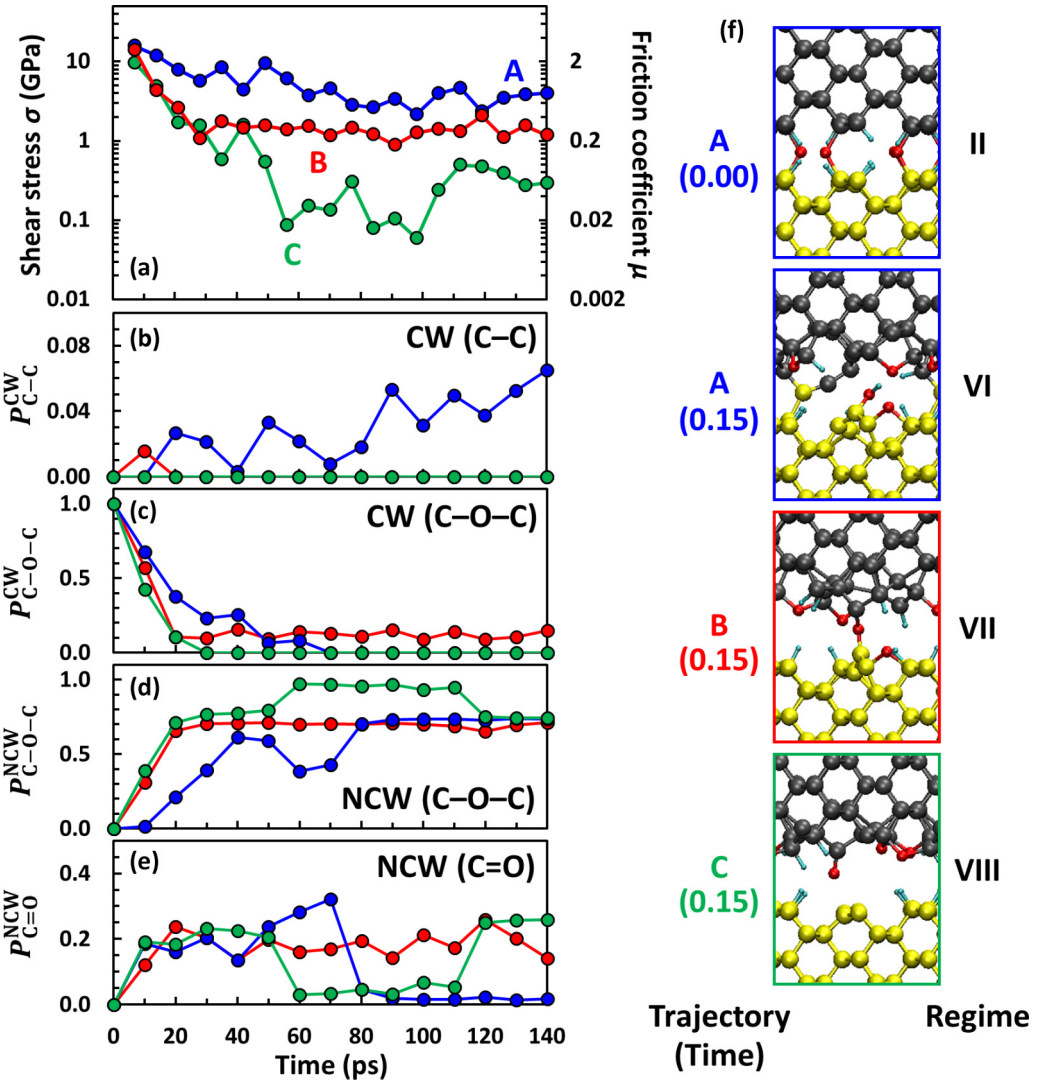

FIG. 2. Friction of water-lubricated diamond (110) surfaces with $n_{H_2O} = 4$. (a) Evolution of frictional shear stresses σ and friction coefficients μ for three independent trajectories (A–C). (b) Evolution of cold-welding C–C bonding and (c)–(e) oxygen functional groups. In (c)–(e), the 10-ps-averaged probabilities P^{CW}_{C-C}, P^{CW}_{C-O-C}, P^{NCW}_{C-O-C}, and $P^{NCW}_{C=O}$ to detect an interfacial C–C bond, an interfacial C–O–C ether group, a passivating C–O–C ether group on one surface, and a passivating keto C=O group are plotted. The same color coding as in (a) is used. (f) Interfacial structures of trajectory A before and after 0.15 ns sliding as well as of B and C after 0.15 ns sliding. Gray and yellow spheres represent C atoms that initially belong to the top and bottom diamond (110) surface, respectively.

same harsh ether-CW regime (regime II with large shear stress $\sigma \sim 10$ GPa), where four interfacial ether groups connect the two diamond (110) surfaces [see starting configuration of trajectory A in Fig. 2(f)]. Upon further sliding each trajectory establishes a different friction regime. The shear stress σ of trajectories A and B decreases only slightly within 0.15 ns sliding time [Fig. 2(a)] indicating a mild CW: trajectory A ends in regime VI with $\sigma \sim 4$ GPa and trajectory B in regime VII with $\sigma \sim 1$ GPa [Fig. 1(d)]. Conversely, the shear stress of trajectory C drops considerably to values $\sigma \sim 0.2$ GPa that are characteristic of the NCW regime VIII [Fig. 1(d)]. In the following sections, the three regimes VI–VIII are scrutinized by looking at the evolution of 10-ps-averaged probabilities of cold-welding C–C bonds P^{CW}_{C-C} [Fig. 2(b)], cold-welding ether groups P^{CW}_{C-O-C} [Fig. 2(c)], passivating ether groups on one surface P^{NCW}_{C-O-C} [Fig. 2(d)], and passivating keto groups $P^{NCW}_{C=O}$ [Fig. 2(e)]. The strong correlation between σ and P and how these regimes are developed are presented.

(a) Mild CW and amorphization (regime VI). Trajectory A represents a characteristic case for regime VI. The two diamond (110) surfaces are initially in regime II (harsh ether-CW) with mobile interfacial O and H atoms [Fig. 2(f)]. Local depletion of H and O gives rise to the formation of C–C bonds between the two (110) surfaces (cold-welding C–C bonds). The curves in Fig. 2(b) show the evolution of the probability p^{CW}_{C-C} to form such a bond (cold-welding C–C bond). For trajectory A, the formation of a cold-welding C–C bond [Fig. 2(b), blue curve] allows a surface C atom to be pulled out of its lattice position [the top yellow atom in Fig. 2(f), at $t = 0.15$ ns of trajectory A]. Usually such an event marks the onset of amorphization [4]. However, the presence of H atoms and oxygen functional groups in the form of hydroxyl, ether, and keto groups [see

Figs. 2(c)–2(e) for the probabilities to find cold-welding ether, passivating ether, or passivating keto groups] mitigate the formation of additional cold-welding C–C bonds and preserve surface crystallinity [A in Fig. 2(f) at $t = 0.15$ ns]. As a result, the number of cold-welding C–C bond remains small thus giving rise to a shear stress ($\sigma \sim 4$ GPa) that is moderate if compared with the harsh CW regime ($\sigma \sim 10$ GPa in regime I) with its high number of cold-welding C–C bonds.

(b) Mild ether-CW (regime VII). Within the first 20 ps of sliding, trajectory B exhibits a transition into the mild ether-CW regime (regime VII). This friction regime is characterized by the absence of cold-welding C–C bonds [$P^{\mathrm{CW}}_{\mathrm{C-C}} = 0$ at all times in Fig. 2(b)] and the presence cold-welding ether groups [$P^{\mathrm{CW}}_{\mathrm{C-O-C}} > 0$ in Fig. 2(c)] with a surface density that is lower than in regime II. A cold-welding C–C bond can be strong enough to break three surface C–C bonds and remove a surface C atom from its lattice position [4], thus leading to the amorphization of the sliding interface. Conversely, in regime VII amorphization is prevented because a cold-welding C–O–C bond can break only the weak C–C bond that connects the zigzag aromatic chain of the (110) surface with the underlying crystal [38].

For trajectory B we observe the presence of three passivating ether groups [red line in Fig. 2(d)] and of one keto group on the upper surface. The π bond of the keto group is easily disrupted due to contacts with the reactive counter surface and

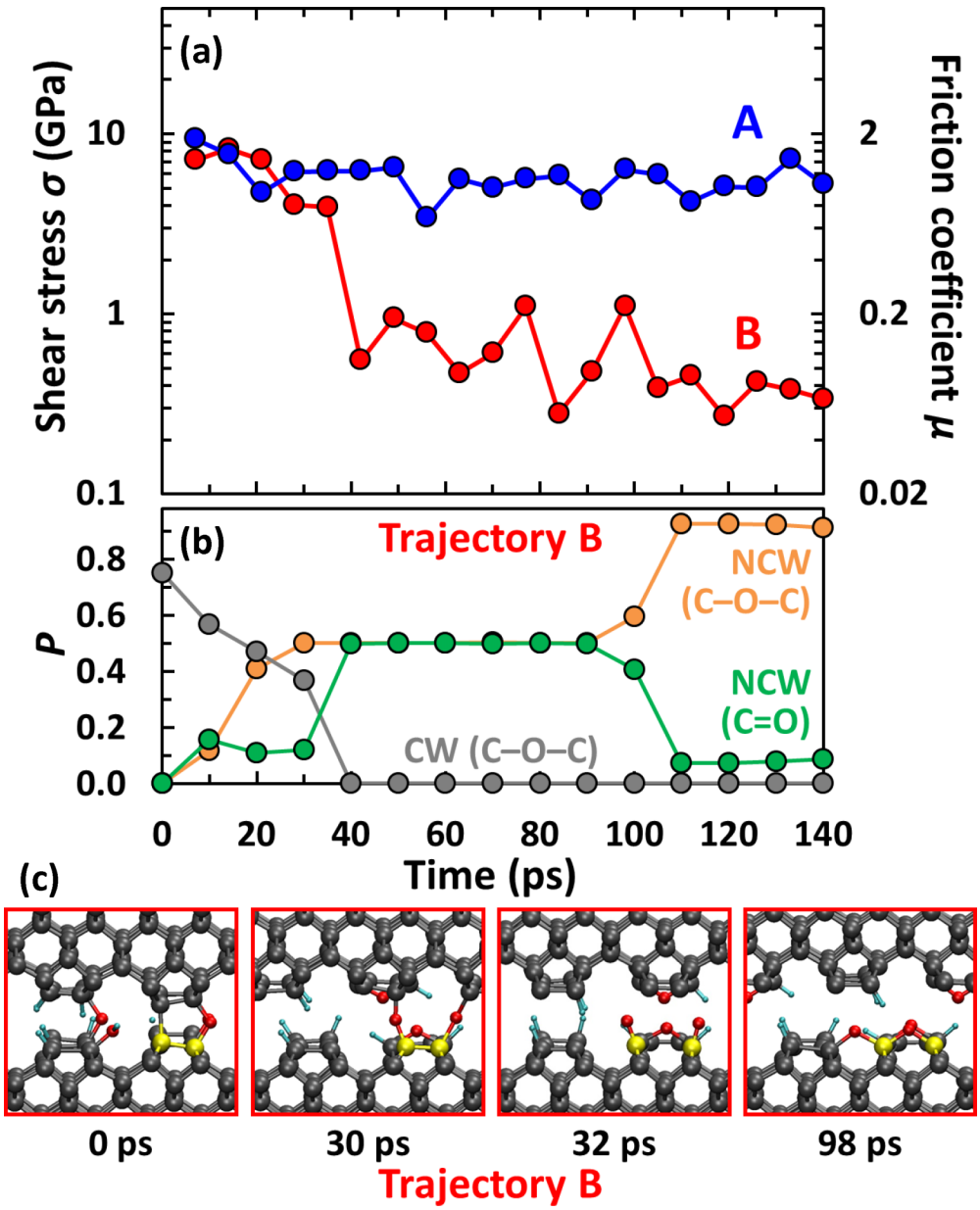

FIG. 3. Friction of water-lubricated diamond (001) surfaces with $n_{\mathrm{H_2O}} = 4$. (a) Evolution of frictional shear stresses σ and friction coefficients μ for two independent trajectories in different sliding directions: $\langle 1\bar{1}0\rangle$ for trajectory A and $\langle 1\bar{1}0\rangle$ for trajectory B. (b) Evolution of oxygen functional groups for trajectory B. In (b), the 10-ps-averaged probabilities $P^{\mathrm{CW}}_{\mathrm{C-O-C}}$, $P^{\mathrm{NCW}}_{\mathrm{C-O-C}}$, and $P^{\mathrm{NCW}}_{\mathrm{C=O}}$ to detect an interfacial C–O–C ether group, a passivating C–O–C ether group on one surface, and a passivating keto C=O group are plotted. (c) Snapshots of trajectory B show the evolution of interfacial structures. The yellow spheres represent a carbon dimer for the sake of visibility.

replaced by a C–O bond, which leads to the formation of a C–O–C binding the two surfaces. However, as soon as one of the two C–O bonds of this cold-welding ether group breaks, the keto group reforms. The periodic transition between keto and interfacial ether groups leads to the occurrence of both groups with significant probability [red lines of Figs. 2(c) and 2(e)] and a resulting reduced $\mu \sim 0.2$.

(c) Keto/ether passivation (regime VIII). Trajectory C ends in an ultralow friction regime that is established by keto/ether surface passivation of the (110) surfaces. The shear stress σ drops rapidly to ~ 0.1 GPa [green curve in Fig. 2(a)] due to the formation of surface passivating keto and ether groups [green curves in Figs. 2(d) and 2(e)] that prevents cold-welding C–C and C–O–C bonding [green curves in Figs. 2(b) and 2(c)].

3. Keto/ether passivation regime (regime VIII) for (001) surfaces

The keto/ether passivation regime (regime VIII in Fig. 1) is also observed for (001) surfaces. Figure 3(a) displays the evolution of shear stress σ and friction coefficient μ of two independent trajectories (A and B) with $n_{H_2O} = 4$ water molecules between two diamond (001) surfaces sliding along different directions ($\langle 1\bar{1}0\rangle$ and $\langle 110\rangle$ for trajectories A and B, respectively). Both trajectories start from the same harsh ether-CW regime (regime II with large shear stress $\sigma \sim 10$ GPa). While trajectory A exhibits no transition within 0.15 ns sliding time, trajectory B undergoes a transition from the harsh ether-CW to keto/ether passivation regime ($\sigma \sim 0.3$ GPa). The evolution of probability for the three types of oxygen functional groups is shown for trajectory B in Fig. 3(b) and representative snapshots are shown in Fig. 3(c). The first panel of Fig. 3(c) displays the starting configuration of trajectory B, where the two diamond (110) surfaces are connected via a C–C bond and three C–O–C bonds. The probability of cold-welding C–O–C bonds P^{CW}_{C-O-C} decreases rapidly from 0.75 ($t = 0$ ps) to 0.00 ($t = 40$ ps) while the probabilities of passivating C–O–C ether (P^{NCW}_{C-O-C}, orange line) and C=O keto ($P^{NCW}_{C=O}$, green line) bonds increase. The increase of P^{NCW}_{C-O-C} at $t < 30$ ps is due to the insertion of O atoms between dimerized surface C atoms that results in breaking of horizontal C–C bonds [second panel in Fig. 3(c)]. At the same time, two cold-welding ether bonds form between two C atoms of a surface carbon dimer (highlighted in yellow) and two C atoms of the counter surface. When the upper two C–O bonds break due to the shear strain, the horizontal C–C bond of the yellow carbon dimer breaks, leading to the formation of two keto groups on the lower surface [third panel in Fig. 3(c)]. A second increase of P^{NCW}_{C-O-C} ($t \approx 100$ ps) is due to transformation of these keto groups into on-surface ether groups. While keto groups give rise to a large oscillation of the shear stress ($0.3 \leqslant \sigma \leqslant 1.0$), their transformation into on-surface ether groups results in a stable low friction ($\sigma \sim 0.3$ GPa).

In summary, for all three low-index diamond surfaces, small traces of water lead to the development of surface-specific friction regimes. This result indicates that the triboreactivity, and in turn the frictional behavior, of these surfaces depend on the geometric arrangement of the carbon atoms with respect to the surface orientation and the sliding direction. This determines the reactivity and coordination of surface carbon atoms, the stability of different C/O/H surfaces and interface groups that can lead to different distances between sliding surfaces, and the presence of surface reconstructions. Moreover, it also determines the strength of the bonds that link surface C atoms to the bulk (this plays a crucial role in, e.g., the formation of stable keto groups or keto radicals). For (110) surfaces, two intermediate friction regimes (regimes VI and VII, $0.2 < \mu < 1.0$) are observed. Since C–C bonds are most easily disrupted on the softest surface [4,26], depending on the density of interfacial bonds, diverse interfacial structures can be developed. For (110) and (001) surfaces, hydroxyl groups are no longer the only form of oxygen that is able to chemically passivate them, and additional keto and ether groups are responsible for their frictional behavior at low water densities.

IV. DISCUSSION

The results demonstrate how the frictional behavior of water-lubricated, low-index diamond surfaces is influenced by the surface orientation. After running-in, oxidized carbon layers on the diamond surfaces retain the crystal structure of the clean surfaces and are responsible for surface-orientation-dependent friction regimes (regimes III and VI–VIII). In the following section, questions arising from our observations are discussed in order to better understand the underlying mechanisms.

A. Why is aromatic passivation unique to the (111) surface?

On clean diamond surfaces, aromaticity can occur by delocalization of p_z electrons in π-bonded zigzag carbon chains. The dimerized (001) surface represents an exception, since π bonds are localized on each carbon dimer and bond lengths are almost the same as those of a typical C=C double bond (1.38 Å). In contrast, (110) and Pandey-reconstructed (111) surfaces possess zigzag chains with delocalized π-bonded electrons. Since the nonreconstructed (111) surface is terminated by carbon atoms with DBs, it can lower its energy by saturating the DBs via a zigzag surface reconstruction with aromatic electron surface states [42]. The ideal (110) surface has already π-bonded zigzag chains and does not show any apparent reconstruction. Both surface geometries are quite similar and the bond lengths of 1.43–1.44 Å are comparable to those of graphene. The geometrical difference is that the Pandey reconstruction alters the topology of the top bilayer from six-membered rings to five- and seven-membered rings, but the (110) surface keeps the six-membered ring topology of the bulk. DFT calculations by Petrini *et al.* [44] revealed a major difference in their electronic structures. A pronounced reactivity of the unreconstructed (111) surface is manifested by a large peak around the Fermi level of the density of states (DOS) (derived from C $2p$ orbitals) due to reactive character of the DBs. However, the peak is not observed for the Pandey-reconstructed (111) surface. The energies of the $2p$ orbitals around the Fermi level are lowered due to the delocalization of π electrons, resulting in a less reactive surface. In contrast, despite its aromatic character, the DOS of the (110) surface has a large peak at the Fermi level reminiscent of the DOS for the nonreconstructed (111) surface. Since such frontier orbitals are generally involved in chemical reactions, the (110) surface is more reactive than the Pandey reconstructed (111)

surface. This difference in electronic structures makes the aromatic passivation (regime III) unique to the (111) surface. The Pandey-reconstructed (111) surface is chemically inert and able to withstand sizable mechanical loads. For instance, dissociative chemisorption of a water molecule on the Pandey-reconstructed (111) surface is impeded by a high activation energy of 1.51 eV [45] and requires normal loads exceeding 6 GPa [11].

B. Why is keto/ether passivation unique to (110) and (001) surfaces?

Keto and ether groups govern the frictional behavior of (110) and (001) surfaces in the presence of trace moisture, but they are less likely to be observed for (111) surfaces. The reason is discussed by looking at the energetics of their formation on the clean surfaces. Formation energies E_f of keto and ether groups on the low-index diamond surfaces are calculated as $E_f = E_{\mathrm{ad}} - (2\mu_{\mathrm{O}} + E_{\mathrm{clean}})$ within SCC-DFTB. Here E_{ad} is the total energy of a diamond surface with two keto or ether groups and E_{clean} is the total energy of the corresponding clean diamond surface. The chemical potential of oxygen μ_{O} is defined as $\frac{1}{2}E_{\mathrm{O}_2}$, where E_{O_2} is the total energy of an isolated oxygen molecule in its triplet state within spin-polarized DFTB [46]. For the (111) surface, the formation energies of keto (E_f^{keto}) and ether (E_f^{ether}) groups are -1.84 and -1.52 eV/atom, respectively. These energies are significantly larger on the other two surfaces. For the (110) surface, E_f^{keto} and E_f^{ether} are -2.38 and -2.07 eV/atom and for the (001) surface E_f^{keto} and E_f^{ether} are -3.00 and -2.22 eV/atom, respectively. The clear ordering between the three surfaces shows that the keto and ether groups are more energetically favorable on the (110) and (001) surfaces than on the (111) surface.

The formation of keto groups requires twofold coordinated C atoms. On the nonreconstructed (111) surface, there are no sites available for divalent oxygen and only keto radicals that cannot passivate the surface can form. An ether group can form when two threefold coordinated carbon atoms are close enough to be bridged by an oxygen atom. On the nonreconstructed (111) surface two neighboring C atoms with DBs have a distance of 2.53 Å—slightly longer than the distance in typical ether compounds (for instance 2.35 Å in dimethylether). However, at the ether oxygen site, two of three C–C–O bond angles deviate from the ideal tetrahedral bond angle (109.5°) by about 25°. Obviously this bond angle strain results in an energetic penalty that mitigates the formation of NCW ether groups and diamond (111). In contrast, the keto radical occupies the tetrahedral site of a surface C atom. Therefore, the keto radical is more energetically favored than the ether form (in agreement with DFT results by Petrini *et al.* [47]). However, in a tribological contact, NCW ether groups and keto radicals on one (111) surface are immediately replaced by CW ether groups (with $E_f^{\mathrm{CW-ether}} = -3.77$ eV/atom) leading to a transition from a NCW to a CW situation. This only happens if on the opposing surfaces C radical sites are available that are able to accept the CW ether bonds. Only if the counter surface is completely passivated NCW ether group and keto radicals are energetically stabilized. Indeed, we observed them in regime III, when the counter surface was Pandey reconstructed.

For the (110) and (001) surfaces, sliding-induced C–C bond breaking creates chemisorption sites for keto and ether oxygen, and as a result, develops the keto/ether passivation regime that retains the characteristics of the pristine surfaces after high-friction running-in. A carbon atom of the (110) surface has one DB, like the nonreconstructed (111) surface. While the minimum distance between carbon atoms from two neighboring zigzag rows is 3.13 Å, the C–C–O bond angles are much closer to the ideal tetrahedral bond angle. Consequently an ether C–O–C group can form between them and stay stable. The energetics is sensitive to the surrounding configuration since energy losses due to the disruption of aromatic chains must be compensated by adsorption energies of either O or H atoms.

The formation of keto oxygen on the (110) surface is not spontaneous but a result of mechanochemistry. A carbon atom on a zigzag row initially has one weak and two strong C–C bonds [4,38]. In the presence of cold-welding C–O–C ether bonds (regime II), shear induces the breaking of the weak C–C bond resulting in the flipping of a horizontal C–C–C segment of the zigzag in a vertical direction and the formation of a twofold coordinated C atom [configuration I of Fig. 4(b)] that is available for the formation of a keto group.

On the clean (001) surface, the dimer reconstruction is energetically more favorable than the ideal surface, since the dimerized C atoms are saturated with two single C–C bonds and one double C=C bond. Here ether bonds form either on dimers (accompanied by the rupture of the horizontal C=C bond) or between dimers of two neighboring rows. The rupture of the horizontal C=C bond on a carbon dimer leads to chemisorption sites that can host keto groups. Contrary to the (110) surface, the formation of keto oxygen on the (001) surface is not a consequence of mechanochemistry, but is due to oxygen divalency and the nature of the dimerized (001) surface. All three forms of oxygen passivation (on-dimer and trans-dimer ether, and keto) can be observed during our MD trajectories [Fig. 3(c)]. The surface passivation with keto and ether oxygen transforms the dimerized surface to the pristine nondimerized one. The relative stability between them as a function of oxygen coverage was studied by Petrini and Larsson with DFT calculations [47]. Their results are in agreement with our DFTB-MD calculations.

C. Why is the mild CW regime only observed for the (110) surface?

In the mild CW regime (regime VI), both diamond surfaces are mostly passivated by hydrogen, hydroxyl, and ether groups, and only small surface patches exhibit carbon atoms with DBs [see Figs. 1(d) and 2(f)]. The chemisorption of the passivating functions results in an increased separation of the two tribopartners [especially for hydroxyl groups—see Fig. 1(d), regime IV]. If diamond surfaces remained completely crystalline, the minimum distance between carbon DB sites would be too large for the formation of C–C bond across the sliding interface. Therefore, the mild CW regime is related to the formation of local defects in the diamond lattice [see Fig. 2(f)] that result in protruding carbon clusters. These clusters sufficiently narrow down the gap between both tribopartners and thus allow for intersurface C–C bonding. It is well known that the sliding

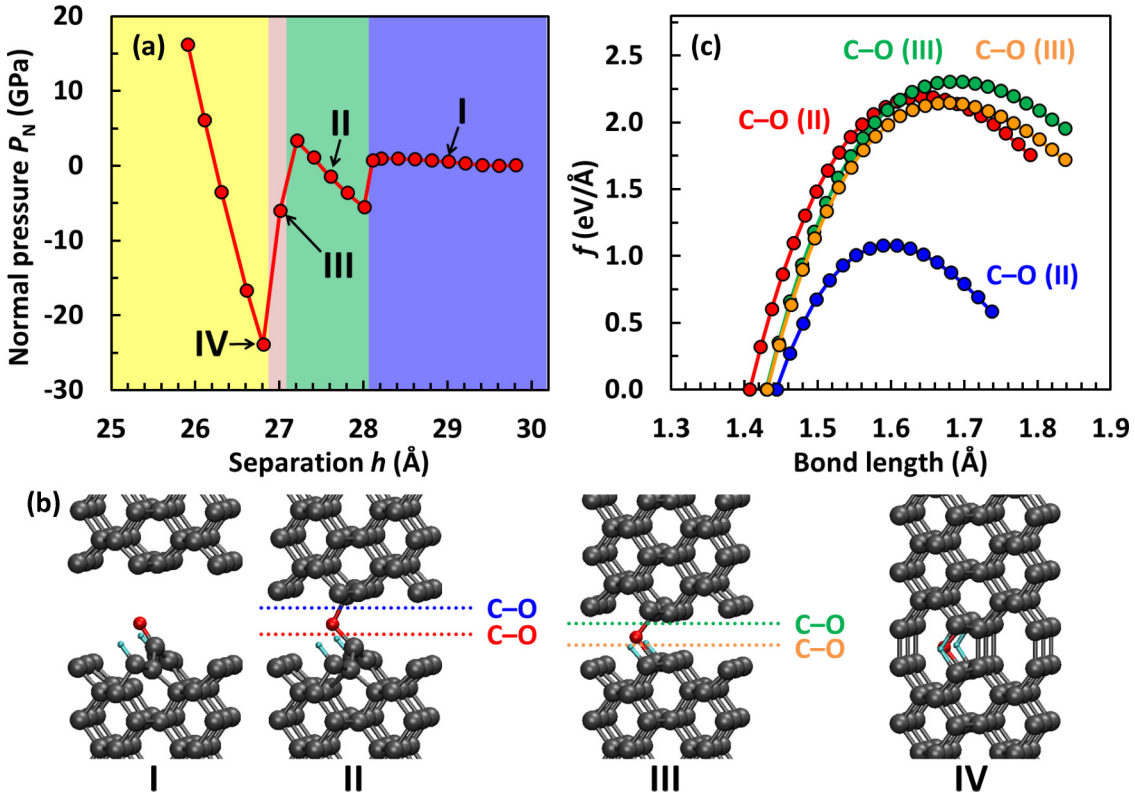

FIG. 4. DFT calculations of two diamond (110) surfaces with $n_{H_2O} = 1$. (a) Normal pressure P_N as a function of the separation h between two rigid layers. (b) Representative structures for each regime highlighted in different color [corresponding to positions I to IV in (a)]. (c) Approximate bond strengths of C–C and C–O bonding. For B and C, the two rigid blocks are separated by different cutting planes in a step of 0.02 Å [shown in configurations II and III in (b)]. Forces along z axis on terminal C atoms bonded initially with O atoms are plotted as a function of bond lengths.

of the (110) surface along the ⟨001⟩ direction results in the largest amorphization rate [4] and therefore the C atoms on (110) surfaces in regime II are most easily removed from their lattice positions [see trajectory A in Fig. 2(f)] and reorganized into carbon nanoasperities [Fig. 1(d)]. Since the presence of certain amounts of H atoms and oxygen functional groups mitigates the formation of additional cold-welding C–C bonds, further removal of C atoms and thus a complete cold welding is inhibited. This leads to a low density of interfacial C–C bonds and yields lower friction than in the harsh CW regime (regime I). The (001) and (111) surfaces are harder to polish and consequently the formation of localized carbon nanoasperities is strongly suppressed. For these two surfaces, defect formation at the diamond interface occurs at such low water densities that harsh CW is inevitable.

D. Why is the mild ether-CW regime only observed for the (110) surface?

The mild ether-CW regime for (110) surfaces is linked to keto groups on vertically flipped surface C–C–C groups and to a transition between passivating keto and cold-welding C–O–C ether groups. In this case, the π bond of a keto group is ruptured and replaced by a C–O bond. The behavior of such a keto group under external loads is elucidated with high-accuracy DFT calculations (Fig. 4). We use the same diamond (110) tribopair as in our DFTB models and start with configuration I in Fig. 4(b), where one of the surfaces is occupied by a keto group on a vertically flipped C atom and two H atoms (assuming that these chemisorbed species originate from a water molecule). Next, the unpassivated upper block is moved down in steps of 0.2 Å. At each position, the system (except for the outer rigid layers) is allowed to relax. Figure 4(a) shows the normal pressure P_N as a function of the separation h between the two rigid layers. In configuration I, the keto group on the flipped C atom is still stable. As the two surfaces are further approaching, the keto group is destabilized and a C–O–C bond forms across the interface (configuration II, $P_N < 1.0$ GPa), resulting in mild ether CW. Note that this C–O–C group possesses a pronounced asymmetry with a bond length of 1.41 Å for the lower and of 1.44 Å for the upper C–O bond. During a further decrease of h, the vertically flipped C–C–C unit is pushed back to its original horizontal position (configuration III, $P_N > 3.3$ GPa). This results in a stable ether group, where both C atoms are fourfold coordinated and both C–O bonds have equal bond length (1.43 Å). If h is further reduced, cold-welding C–C bonds form all over the interface between the two surfaces (configuration IV).

These simulations indicate that for the (110) surface, a keto group on a flipped C atom is able to survive only at low contact pressures. During sliding, such keto groups can collide with carbon atoms in the counter body leading to local high contact pressures that easily cause a transition to ether-CW (configuration II or III). Two types of the cold-welding ether

groups are found in Fig. 4(b): the asymmetric configuration II and the symmetric configuration III. In configuration II the O atom is bonded to twofold and threefold coordinated C atoms (asymmetric), whereas in configuration III it binds to two threefold coordinated C atoms(symmetric). Additional DFT calculations in Fig. 4(c) show that the asymmetric ether group in configuration II is responsible for the mild ether-CW regime (regime VII) due to different bond strengths of the two C–O bonds. Figure 4(c) shows the force/bond-distance curves for the four C–O bonds of configurations II and III in Fig. 4(b). For both configurations, two different blocks of atoms are defined [separated by the respective dotted line in Fig. 4(b)] and these blocks are rigidly separated while the absolute values of forces along z axis on the terminal C atoms of the C–O bonds are recorded. A similar approach has been employed in a previous study [38]. The strengths of the two C–O bonds in configuration III are almost the same ($f_{\mathrm{C-O}}^{\max} = 2.2$–$2.3\ \mathrm{eV/\AA}$), whereas in configuration II the upper C–O bond is only half ($f_{\mathrm{C-O}}^{\max} = 1.1\ \mathrm{eV/\AA}$) as strong as the lower one ($f_{\mathrm{C-O}}^{\max} = 2.2\ \mathrm{eV/\AA}$). The asymmetric C–O bond strengths lead to the preferential breaking of the weaker, upper C–O bond and results in lower shear forces. Moreover, the vertical orientation of the C–C–C group atom separates two diamond surfaces enough to prevent the formation of additional cold-welding C–C bonds.

As discussed in the previous section, the formation of keto groups on the (001) surface requires the rupture of horizontal C–C bonds on carbon dimers. Keto groups can form only in the case where both C atoms are occupied with an O atom [see a typical example in Fig. 3(c)]. The cleaved horizontal C–C bond reforms as soon as the π bonds of the two keto groups (e.g., due to a high local contact pressure) are replaced by two cold-welding C–O–C ether bonds. Thus, the structure of the (001) surface inhibits asymmetric ether groups. Therefore, keto oxygen on the (001) surface is not a precursor for mild ether-CW and plays merely a role in regime VIII as a passivating functional group.

V. SUMMARY AND CONCLUSIONS

Employing large-scale QM MD simulations, we elaborate a map of the friction regimes for water-lubricated, low-index diamond surfaces. Extreme water starvation on the one hand and water-rich conditions on the other hand result in four universal friction regimes that can be observed for all low-index surfaces irrespective of the sliding direction. Water starvation results in regime I—cold welding accompanied by amorphization and regime II—crystalline systems cold welded via ether bridges. Water-rich conditions lead to two non-cold-welding regimes: regime IV—passivation via hydroxyl groups and hydrogen and regime V—OH/H passivation and formation of a nm-thin, layered water film.

However, when the amount of lubricating water lies between starvation and water-rich conditions we observe four additional sliding regimes that are not universal, i.e., trace moisture leads to surface-orientation-dependent friction mechanisms. Passivation by an aromatic surface reconstruction (regime III) is unique to the (111) surface, and establishes an ultralow friction regime that does not rely on chemical terminations. For the (110) surface, the anisotropic resistance to shear attributed to the nonequivalent C–C bond strengths on the (110) surface leads to diverse surface morphologies and functionalities: mild CW (regime VI), mild ether-CW (regime VII), and keto/ether passivation (regime VIII). The keto/ether passivation regime can also be observed for (001) surfaces. On both surface orientations, regime VIII leads to ultralow friction.

In conclusion, the characteristic structural patterns and oxygen functional groups for each surface orientation are responsible for their different frictional behavior in water lubrication. Our results are qualitatively supported by state-of-the-art spectroscopic measurements of UNCD [14] and a-C surfaces [18]. However, to the best of our knowledge, there are no experimental studies in which highly resolved analytical techniques are applied to single-crystal diamond surfaces with different surface orientations under technologically relevant conditions. We therefore hope that this work will stimulate such experimental activities as well as further simulation studies. Our findings should be useful not only for the control of tribological properties of MCD but also for the modeling of realistic oxygen-functionalized surfaces with nonreactive force fields [48] and a comprehensive understanding of frictional anisotropy of single-crystal diamond [20]. Moreover, since water is the simplest oxygen-containing lubricant, these findings should be helpful to predict friction mechanisms of carbon-based tribocoatings (such as MCD and tetrahedral a-C) lubricated with other common oxygen-containing lubricant molecules (such as glycerol [28] and oleic acid [12]). Of recent particular interest is superlubricity of tetrahedral a-C in boundary or mixed lubrication triggered by the formation of either oxidized graphitic tribolayers [12] or chemical passivation layers with H/OH groups [18]. The former could be a generalized regime III, where an aromatic tribolayer protects a-C surfaces from harsh CW accompanied by further amorphization, rehybridization, or plastic deformation. Hence, this study opens new perspectives for atomic-scale control and manipulation of nanoscale oxidized tribofilms supported by carbon surfaces.

ACKNOWLEDGMENTS

T.K. acknowledges financial support by JSPS Overseas Research Fellowships. G.M. and M.M. acknowledge funding from the industrial board of the MicroTribology Center μTC. We are grateful for computing time on the supercomputers JURECA at Jülich Supercomputing Centre (Grant HFR09) and NEMO at the University of Freiburg.

[1] S. W. Zhang, Friction **1**, 186 (2013).
[2] K. Holmberg, P. Andersson, and A. Erdemir, Tribol. Int. **47**, 221 (2012).
[3] J. S. McFarlane and D. Tabor, Proc. R. Soc. London Ser. A **202**, 244 (1950).
[4] L. Pastewka, S. Moser, P. Gumbsch, and M. Moseler, Nat. Mater. **10**, 34 (2011).
[5] Y. Liu and I. Szlufarska, Phys. Rev. Lett. **109**, 186102 (2012).

[6] C. Matta, L. Joly-Pottuz, M. I. De Barros Bouchet, J. M. Martin, M. Kano, Q. Zhang, and W. A. Goddard, III, Phys. Rev. B **78**, 085436 (2008).
[7] Q. Li, Y. Dong, D. Perez, A. Martini, and R. W. Carpick, Phys. Rev. Lett. **106**, 126101 (2011).
[8] A. Erdemir and C. Donnet, J. Phys. D: Appl. Phys. **39**, R311 (2006).
[9] R. W. Carpick and M. Salmeron, Chem. Rev. **97**, 1163 (1997).
[10] B. Bhushan, J. N. Israelachvili, and U. Landman, Nature (London) **374**, 607 (1995).
[11] T. Kuwahara, G. Moras, and M. Moseler, Phys. Rev. Lett. **119**, 096101 (2017).
[12] M. I. De Barros Bouchet, J. M. Martin, J. Avila, M. Kano, K. Yoshida, T. Tsuruda, S. Bai, Y. Higuchi, N. Ozawa, M. Kubo, and M. C. Asensio, Sci. Rep. **7**, 46394 (2017).
[13] M. I. De Barros Bouchet, G. Zilibotti, C. Matta, M. C. Righi, L. Vandenbulcke, B. Vacher, and J. M. Martin, J. Phys. Chem. C **116**, 6966 (2012).
[14] A. R. Konicek, D. S. Grierson, P. U. P. A. Gilbert, W. G. Sawyer, A. V. Sumant, and R. W. Carpick, Phys. Rev. Lett. **100**, 235502 (2008).
[15] A. Schade, S. M. Rosiwal, and R. F. Singer, Diam. Relat. Mater. **15**, 1682 (2006).
[16] J. Otschik, A. Schrüfer, J. Thelke, M. Kirchhof, and S. Schmaderer, World Pumps **2010**, 18 (2010).
[17] M. Seal, Proc. R. Soc. London Ser. A **248**, 379 (1958).
[18] A. R. Konicek, D. S. Grierson, A. V. Sumant, T. A. Friedmann, J. P. Sullivan, P. U. P. A. Gilbert, W. G. Sawyer, and R. W. Carpick, Phys. Rev. B **85**, 155448 (2012).
[19] G. Zilibotti, S. Corni, and M. C. Righi, Phys. Rev. Lett. **111**, 146101 (2013).
[20] F. P. Bowden and D. Tabor, *The Friction and Lubrication of Solids Part II* (Oxford University Press, London, 1964).
[21] F. P. Bowden and J. E. Young, Proc. R. Soc. London Ser. A **208**, 444 (1951).
[22] D. Porezag, T. Frauenheim, T. Köhler, G. Seifert, and R. Kaschner, Phys. Rev. B **51**, 12947 (1995).
[23] M. Elstner, D. Porezag, G. Jungnickel, J. Elsner, M. Haugk, T. Frauenheim, S. Suhai, and G. Seifert, Phys. Rev. B **58**, 7260 (1998).
[24] P. Giannozzi, S. Baroni, N. Bonini, M. Calandra, R. Car, C. Cavazzoni, D. Ceresoli, G. L. Chiarotti, M. Cococcioni, I. Dabo, A. Dal Corso, S. de Gironcoli, S. Fabris, G. Fratesi, R. Gebauer, U. Gerstmann, C. Gougoussis, A. Kokalj, M. Lazzeri, L. Martin-Samos, N. Marzari, F. Mauri, R. Mazzarello, S. Paolini, A. Pasquarello, L. Paulatto, C. Sbraccia, S. Scandolo, G. Sclauzero, A. P. Seitsonen, A. Smogunov, P. Umari, and R. M. Wentzcovitch, J. Phys. Condens. Matter **21**, 395502 (2009).
[25] G. Gao, R. J. Cannara, R. W. Carpick, and J. A. Harrison, Langmuir **23**, 5394 (2007).
[26] M. R. Jarvis, R. Perez, F. M. van Bouwelen, and M. C. Payne, Phys. Rev. Lett. **80**, 3428 (1998).
[27] X. Zhang, R. Schneider, E. Müller, M. Mee, S. Meier, P. Gumbsch, and D. Gerthsen, J. Appl. Phys. **115**, 063508 (2014).
[28] C. Matta, M. I. De Barros Bouchet, T. Le-Mogne, B. Vachet, J. M. Martin, and T. Sagawa, Lubr. Sci. **20**, 137 (2008).
[29] L. Pastewka, S. Moser, and M. Moseler, Tribol. Lett. **39**, 49 (2010).
[30] D. Frenkel and B. Smit, *Understanding Molecular Simulations: From Algorithms to Applications*, 2nd ed. (Academic, New York, 2001).
[31] M. P. Allen and D. J. Tildesley, *Computer Simulation of Liquids* (Oxford University Press, Oxford, 1987).
[32] P. E. Blöchl, Phys. Rev. B **50**, 17953 (1994).
[33] J. P. Perdew, K. Burke, and M. Ernzerhof, Phys. Rev. Lett. **77**, 3865 (1996).
[34] H. J. Monkhorst and J. D. Pack, Phys. Rev. B **13**, 5188 (1976).
[35] T. D. B. Jacobs and R. W. Carpick, Nat. Nanotechnol. **8**, 108 (2013).
[36] B. Bhushan, Tribol. Lett. **4**, 1 (1998).
[37] S. A. Adelman and J. D. Doll, J. Chem. Phys. **64**, 2375 (1976).
[38] A. Peguiron, G. Moras, M. Walter, H. Uetsuka, L. Pastewka, and M. Moseler, Carbon N.Y. **98**, 474 (2016).
[39] Y. Leng and P. T. Cummings, Phys. Rev. Lett. **94**, 026101 (2005).
[40] H. Sakuma, K. Otsuki, and K. Kurihara, Phys. Rev. Lett. **96**, 046104 (2006).
[41] E. H. Abramson, Phys. Rev. E **76**, 051203 (2007).
[42] K. C. Pandey, Phys. Rev. B **25**, 4338 (1982).
[43] G. Kern and J. Hafner, Phys. Rev. B **58**, 13167 (1998).
[44] D. Petrini and K. Larsson, J. Phys. Chem. C **112**, 14367 (2008).
[45] G. Levita, S. Kajita, and M. C. Righi, Carbon N.Y. **127**, 533 (2018).
[46] C. Köhler, T. Frauenheim, B. Hourahine, G. Seifert, and M. Sternberg, J. Phys. Chem. A **111**, 5622 (2007).
[47] D. Petrini and K. Larsson, J. Phys. Chem. C **112**, 3018 (2008).
[48] D. Savio, K. Falk, and M. Moseler, Tribol. Int. **120**, 269 (2018).